



# Strongly Depleted Methanol and Hypervolatiles in Comet C/2021 A1 (Leonard): Signatures of Interstellar Chemistry?

Sara Faggi<sup>1,2</sup> , Manuela Lippi<sup>3</sup> , Michael J. Mumma<sup>2,4</sup> , and Geronimo L. Villanueva<sup>2</sup>

<sup>1</sup>American University, 4400 Massachusetts Avenue NW, Washington, DC 20016, USA; [faggi@american.edu](mailto:faggi@american.edu)

<sup>2</sup>NASA Goddard Space Flight Center, 8800 Greenbelt Road, MD 20771, USA

<sup>3</sup>Institute for Geophysics and Extraterrestrial Physics, Technische Universität Braunschweig, Mendelssohnstraße 3, D-38106 Braunschweig, Germany

<sup>4</sup>University of Maryland, 1940 Regents Drive, College Park, MD 20740, USA

Received 2022 September 7; revised 2022 November 21; accepted 2022 November 25; published 2023 January 19

## Abstract

We measured the chemical composition of comet C/2021 A1 (Leonard) using the long-slit echelle grating spectrograph iSHELL/IRTF on 2021 December 20 and on 2022 January 8 and 9. We sampled 11 primary volatiles (H<sub>2</sub>O, HCN, NH<sub>3</sub>, CO, C<sub>2</sub>H<sub>2</sub>, C<sub>2</sub>H<sub>6</sub>, CH<sub>4</sub>, CH<sub>3</sub>OH, H<sub>2</sub>CO, OCS, and HCl) and three product species (CN, NH<sub>2</sub>, and OH) and retrieved their molecular abundances, which can serve as important cosmogonic indicators. The abundance ratios, relative to water, of almost all trace volatiles appear to be depleted relative to reference values, with methanol abundance among the lowest observed in a comet. The observed stronger depletion of CH<sub>3</sub>OH, relative to CO, CH<sub>4</sub>, and C<sub>2</sub>H<sub>6</sub>, could be evidence of an interstellar medium (ISM) chemistry signature in comet/Leonard ices. Both the detection of HCl and the detection of OCS support the idea of interstellar origin for comet/Leonard ices, since they are preferentially formed via solid-phase interstellar chemistry and are then found depleted in dense molecular clouds and protoplanetary disks, suggesting that their abundances in comets might retain a signature from the ISM era. The comet also revealed a complex outgassing pattern, with volatiles largely shifted toward the sunward direction, relative to the dust profiles that appeared centered on the nucleus-centric position. Here we present emission profiles measured along the Sun–comet line for brightest lines of H<sub>2</sub>O, HCN, C<sub>2</sub>H<sub>6</sub>, and CO, and we show that they follow the release of water in similar fashion, interpreting this as indication of a not strict relationship between polar and apolar ices.

*Unified Astronomy Thesaurus concepts:* Long period comets (933); High resolution spectroscopy (2096); Infrared spectroscopy (2285); Comae (271)

## 1. Introduction

The significance of studying comets lies in their astrobiological relevance. Comets are believed to be the well-preserved remnants of the solar system formation, and their chemical investigations provide important hints to understand the evolution of the protoplanetary disk material from which the solar system formed (Mumma & Charnley 2011). Signatures of primordial interstellar chemistry, or signatures of thermal processing at the solar nebula location where such ices formed, may be today preserved in the cometary chemical composition. Therefore, taxonomical studies, based on molecular abundances, allow us to determine important information regarding the nature of the cometary material and its evolution during the different phases of solar system formation. Investigations of molecular mixing ratios in comets allow us indeed to (1) trace the evolution of the volatile reservoirs, (2) investigate the interplay between the refractory and icy components and how they came together to form the first protoplanetary embryos, and (3) study the potential role of comets in delivering water and organics to the barren rocky planets, enabling life to arise.

The gas-rich comet C/2021 A1 (Leonard), hereafter comet/Leonard, was one of the brightest comets to appear in the northern hemisphere since the passages of (gas-rich) C/1996 B2 (Hyakutake) in 1996 and (dust-rich) comet C/1995 O1

(Hale–Bopp) in 1997. The bright dust-rich comet C/2020 F3 (NEOWISE) provided an analog to Hale–Bopp (Faggi et al. 2021, and references therein). The huge advances in astronomical instrumentation since 1996–1997 have enabled profound advances in scientific insights, as outlined herein.

In this paper, we present investigations of the molecular composition of the long-period comet/Leonard conducted with iSHELL at the NASA/IRTF facility. Comet/Leonard was discovered by G. J. Leonard at the Mount Lemmon Observatory on 2021 January 3, when it was at  $\sim 5$  au. It occupied a retrograde orbit that, before entering the inner solar system, had an orbital period of about 92,000 yr ( $1/a = 0.000490$ ; Nakano Note 4621), and so the comet was not dynamically new. Comet/Leonard was 0.233 au from Earth on 2021 December 12, and it made its closest approach to the Sun on 2022 January 3, with a perihelion distance of 0.615 au.

The comet reached an apparent visual magnitude of around 5 in early December, and experienced amateur astronomers first reported it as a naked-eye object by 2021 December 5. The comet experienced numerous outbursts, reaching a magnitude of 3 before dimming to 4 in early January. The Trappist survey of comet/Leonard on every night between December 20 and January 25 revealed that the comet underwent an outburst between January 6 and 8, brightening by 1.5 mag, and all production rates increased by a factor of four (Jehin et al. 2022). The flux started to drop again on UT January 10. Our observations of UT January 8 and 9 fall within this outburst period. The near-perihelion temporal evolution of its visual coma and tail is here further documented by a series of 12

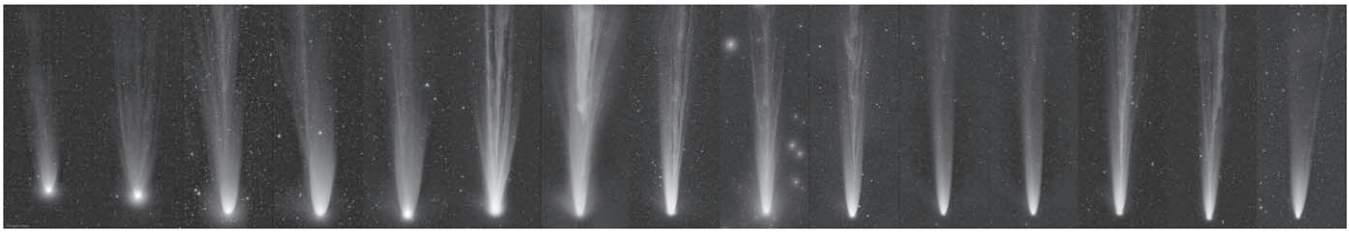


**Figure 1.** Twelve images of comet/Leonard as observed from Skygems, Namibia (Rolando Ligustri, CARA/UAI). From left to right the observations begin on 2021 December 19 with continuity until 2021 December 12; the last two are on 2022 February 1 and 2022 May 1.

**Table 1**  
Comet/Leonard Observing Log

Date	Object Name	Spectral Setting	Exposure Time (s), Coadds	Time on Source (minutes)	Slit Width (arcsec)	Air Mass	$R_h$ (au)	$\Delta$ (au)	$\dot{\Delta}$ (km s <sup>-1</sup> )
20 Dec 2021	BS7773	L1c <sup>a</sup>	60, 1	4	4	1.53	...	...	...
	C/2021 A1	L1c <sup>a</sup>	60, 1	24	0.75	2.21–2.92	0.68	0.42	59.7
22 Dec 2021				Thick clouds					
2 Jan 2022				Snowstorm					
3 Jan 2022				Snowstorm					
8 Jan 2022	C/2021 A1	M1	10,3	68	0.75	1.83–1.78	0.62	1.08	59.8
	C/2021 A1	Lp1c*	60,1	64	0.75	1.80–2.04	0.62	1.08	59.8
	BS8143	Lp1c*	10,1	8	4.0	1.28–1.30	...	...	...
	BS8143	M1	2,10	16	4.0	1.35–1.39	...	...	...
9 Jan 2022	C/2021 A1	L1c*	60, 1	80	0.75	2.02–1.78	0.62	1.12	58.7
	C/2021 A1	L3	60, 1	68	0.75	1.82–2.28	0.62	1.12	58.7
	BS8143	L3	60, 1	8	4.0	1.39–1.43	...	...	...
	BS8143	L1c*	60, 1	8	4.0	1.45–1.54	...	...	...

**Note.**

<sup>a</sup> L1c: setting L1 custom upper wavelengths 3.1  $\mu\text{m}$ . Lp1c: setting Lp1 custom upper wavelengths 3.71  $\mu\text{m}$ .

images collected with the Skygems telescope in Namibia (Figure 1, after Rolando Ligustri, CARA/UAI).

Comet/Leonard disrupted completely by 2022 February 22, 6 weeks after our observations. The unusual, depleted chemistry found by us in comet/Leonard is compared with the composition of C/1999 S4 (LINEAR), another long-period comet that disrupted several weeks after being characterized at infrared wavelengths (Mumma et al. 2001; Lippi et al. 2021). We discuss the prospects that their similar compositions reflect a common origin or merely the overall depletion of selective ices near the end of life.

## 2. Observations and Data Reduction

We observed comet/Leonard with iSHELL, the long-slit near-infrared high-resolution immersion echelle spectrograph available at the NASA IRTF facility. In iSHELL, dispersion is obtained by a silicon immersion grating, and the resolving powers approach about  $\lambda/\delta\lambda = 70,000$  with the 0''375 slit. Six cross-dispersing gratings mounted on a tiltable mechanism permit selection of wavelength ranges over 15 distinct spectral settings (Rayner et al. 2012, 2022).

We planned to follow comet/Leonard as closely as possible during its perihelion approach on three 2-day visits, but due to severe weather conditions, we could observe the object only on 3 days: the first one, before its perihelion passage, on 2021 December 20, when weather conditions allowed us to obtain

only 24 minutes on source, and 2 days right after the perihelion on 2022 January 8 and 9, when the comet was undergoing a major outburst. During this period, the comet was mostly a daytime object with a solar elongation angle that varied (slightly) around 34° for the whole period. Daytime observations are uniquely allowed at IRTF thanks to the superior image guider offered with iSHELL, which provides the possibility of selecting among multiple filters to properly image and effectively guide on the comet. Visibility conditions for comet/Leonard are summarized in Table 1.

To obtain a complete characterization of the outgassing activity and composition of this object, we adopted our usual customized iSHELL spectral settings (L1c, Lp1c), as we discussed and explained in our previous works (Faggi et al. 2018, 2019, 2021), and two standard settings (L3 and M1). These settings permit targeting the nitrile region (2.9–3.0  $\mu\text{m}$ ), especially focusing on detections of HCN, C<sub>2</sub>H<sub>2</sub>, NH<sub>3</sub>, and NH<sub>2</sub> in L1c; the CH<sub>2</sub> and CH<sub>3</sub> stretch region (3.3–3.5  $\mu\text{m}$ ) in Lp1c and L3 targeting HCl, CH<sub>4</sub>, C<sub>2</sub>H<sub>6</sub>, H<sub>2</sub>CO, and CH<sub>3</sub>OH; and CO, CN, OCS, and H<sub>2</sub>O (4.6–5.1  $\mu\text{m}$ ) in M1. Prompt emission from hydroxyl (OH\*), a direct proxy for H<sub>2</sub>O, is sampled in many orders.

During our observations, we oriented the slit position angle (PA) along the extended Sun–comet radius vector direction (see Table 2 and Figure 2), and on those dates solar phase angles ranged from 125° on December 20 to 63°–61° in early January, so the heliocentric radius vector (the Sun-to-comet

**Table 2**  
Spatial Profile Information for Primary Volatiles

Date	Spectral Setting	Observing Interval (UTC)	Gas-Dust <sup>a</sup> (pixels)	PsAng <sup>b</sup> (arcsec)	PhAng <sup>c</sup> (deg)	Plate Scale <sup>d</sup> (arcsec pixel <sup>-1</sup> )	$D^e$ (arcsec)	$\Delta^f$ (au)	$\rho^g$ (km)
20 Dec 2021	L1c	03:32:08.3–04:17:01.0	H <sub>2</sub> O: –6 HCN: –6	90	124.8	0.167	2.505	0.42	±382.4
8 Jan 2022	M1	00:07:56.1–00:51:06.2	H <sub>2</sub> O: –1 CO: –2	103	63.5	0.165	2.475	1.08	±971.6
	Lp1c	03:03:57.7–03:11:42.7	C <sub>2</sub> H <sub>6</sub> : –2			0.166	2.490		±977.5
9 Jan 2022	L1c	23:14:34.4–00:43:09.4	H <sub>2</sub> O: –8 HCN: –8	103	60.8	0.167	2.505	1.12	±1019.8
	L3	01:32:18.6–03:04:04.1	C <sub>2</sub> H <sub>6</sub> : –6			0.187	2.805		±1141.9

**Notes.**

<sup>a</sup> Pixels shift between the gas and the dust peaks along the slit.

<sup>b</sup> Slit position angle, set to be the same as the Sun position angle; see Figure 2.

<sup>c</sup> Solar phase angles.

<sup>d</sup> Adopted mean plate scales in the cross-disperser direction.

<sup>e</sup> Spanned arcsecond along the slit.

<sup>f</sup> Geocentric distance to comet.

<sup>g</sup> Corresponding projected nucleocentric distance.

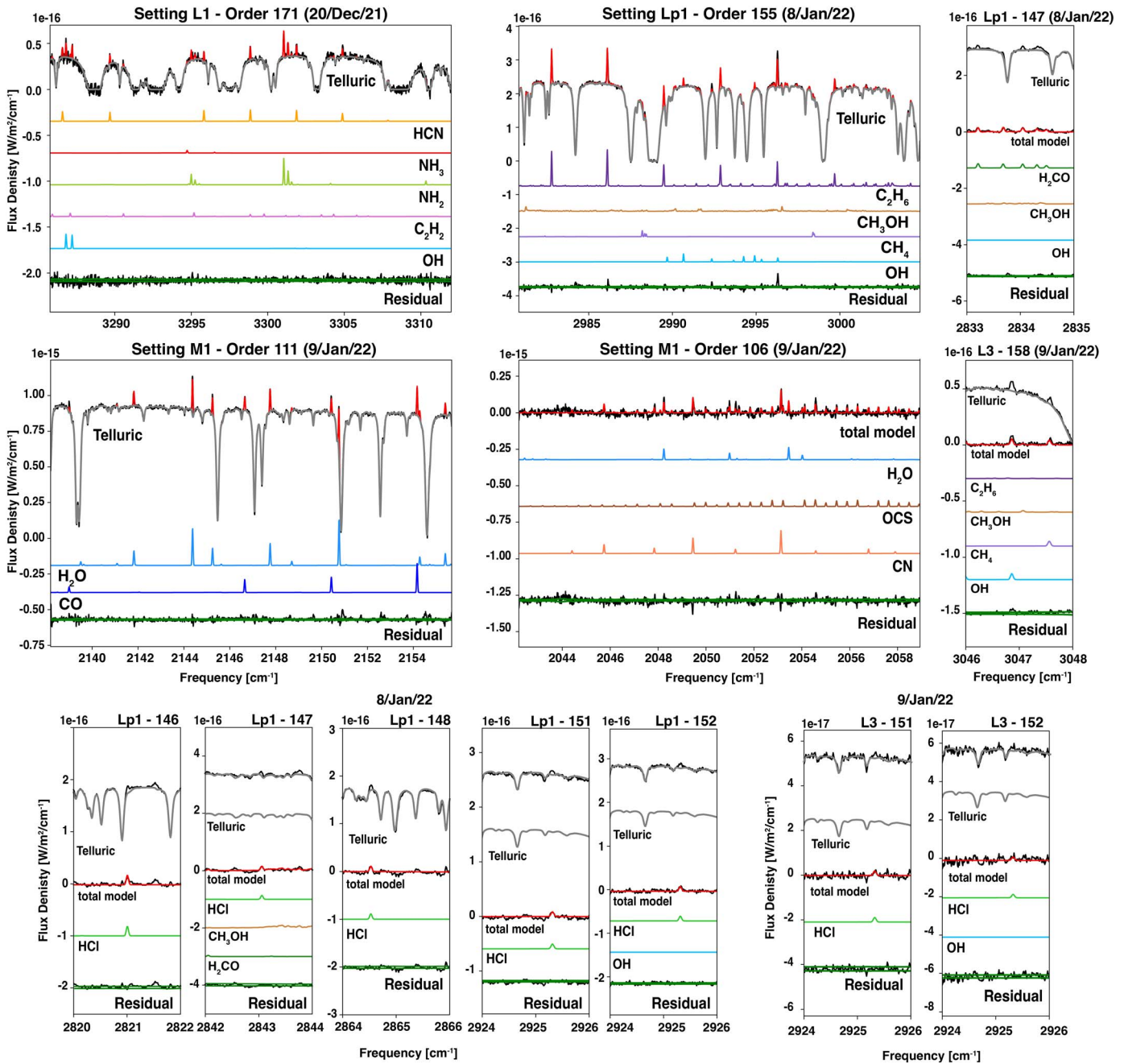


**Figure 2.** Spectra extracted from iSHELL/IRTF. Panels show cometary spectra extracted from specific orders of the four iSHELL echellograms. Cometary spectra are shown and compared with optimized synthetic spectra for detected species. The modeled emission spectra are shown shifted downward along the y-axis relative to the residual cometary spectrum (multiple colors; see text), for clarity. The lowest trace in each panel is the grand residual after subtracting the modeled emissions from the measured molecular residual; the expected stochastic noise envelope ( $\pm\sigma$ ) is shown in light green. The bottom six panels show zoomed-in portions of spectral orders.

line vector) did not lie in the plane of the sky, and the observed spatial profiles are then a projection on such a plane.

Data here presented were processed adopting our IDL-based Goddard standard algorithms for data reduction and analysis (e.g., DiSanti et al. 2006; Villanueva et al. 2012a, 2012b, 2013a), and results were also compared to those obtained with our recently developed data reduction Python package “*spec.py*” to benchmark the new pipeline (G. L. Villanueva et al. 2023, in preparation). Following our usual data processing scheme, for each analyzed order of a spectral setting we proceeded by cropping it, removing bad pixels, then spatially and spectrally straightening it, and finally wavelength- and

flux-calibrating it. As explained in previous works, frequency calibration was achieved by fitting the terrestrial radiance with the Planetary Spectrum Generator (PSG; Villanueva et al. 2018), while flux calibration was obtained by applying the conversion efficiency derived by fitting the top-of-atmosphere stellar flux density ( $\text{W m}^{-2} \text{cm}^{-1}$ ) and the measured instrumental counts per pixel ( $\text{ADU s}^{-1}$ ). We extracted the final calibrated cometary spectra from the signal contained in a rectangular aperture of size  $5 \times 15$  pixels (see Table 2 and Figure 2 for corresponding sampled kilometers).

Examples of cometary spectra extracted from multiple orders across the three observing dates are shown in Figure 2. In the

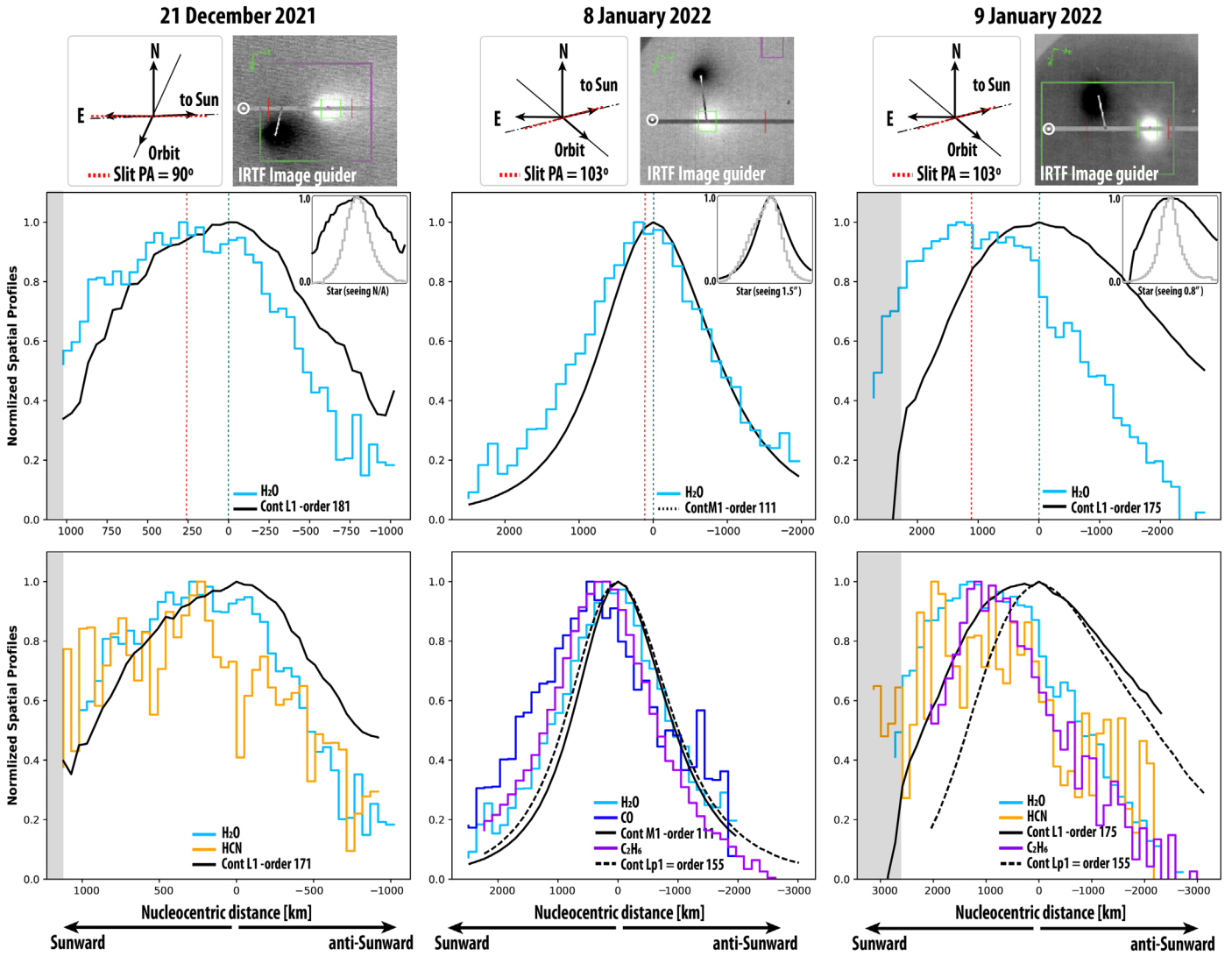


**Figure 3.** Top: the graphics show images of the comet taken by the iSHELL/IRTF image guider (with selected filter at  $3.46 \mu\text{m}$ ) during our observations. The diagram to their left shows a representation of the adopted slit position angles during each observing run. Slit-PA was set along the Sun-to-comet radial direction as projected on the sky plane. Main grid: the grid shows the molecular spatial profiles (water: blue; HCN: orange;  $\text{C}_2\text{H}_6$ : purple) and dust spatial profiles (black dotted) during the observing campaign. Positive  $\rho$ [km] are in the Sun direction. Shaded gray areas mark the regions outside the combination of the A- and B-beams. Beyond this “good” center region, where a proper A–B sky cancellation is obtained, the profiles are more susceptible to systematics and are discarded.

figure, starting from the top left panel, we show order 171 in setting L1c, where detections of HCN (orange),  $\text{NH}_3$  (red),  $\text{NH}_2$  (lime),  $\text{C}_2\text{H}_2$  (pink), and OH (light blue) are highlighted. In the top right panel, we show spectra extracted from order 155 in setting Lp1c where  $\text{C}_2\text{H}_6$  (dark purple), a weak  $\text{CH}_3\text{OH}$  (dark orange),  $\text{CH}_4$  (light purple), and  $\text{OH}^*$  (light blue) are detected. The middle panels show two orders of setting M1; the first one is order 111, where detections of  $\text{H}_2\text{O}$  (blue) and CO (dark blue) are reported, while the second one is order 106, where  $\text{H}_2\text{O}$  (blue), OCS (brown), and CN (pink-salmon) are shown. In the bottom part of the figure, six zoomed-in panels are shown. From left to right, the first two plots show detections of  $\text{H}_2\text{CO}$  (green) in order 147 of setting Lp1c and detections of  $\text{CH}_4$  (light purple), together with weak  $\text{CH}_3\text{OH}$  and OH in order 158 of setting L3. The last four plots show detections of HCl in orders 151 and 152 of settings Lp1c and L3.

We searched for lines of the HCl (1–0) band falling in order 146 (P3 at rest frequency  $2821.568 \text{ cm}^{-1}$ ), in order 147 (P2 at rest frequency  $2865.0978 \text{ cm}^{-1}$ ), in order 148 (P1 at rest

frequency  $2843.624 \text{ cm}^{-1}$ ), in order 151 (R0 at rest frequency  $2906.246 \text{ cm}^{-1}$  and R1 at  $2925.896 \text{ cm}^{-1}$ ), and in order 152 (R1 at  $2925.896 \text{ cm}^{-1}$  and R2 at  $2944.913 \text{ cm}^{-1}$ ). While the line at  $2906.246 \text{ cm}^{-1}$  fell into the telluric absorption, the others were available, and the R1 transition at  $2925.896 \text{ cm}^{-1}$  was detected in both orders, for 2 consecutive days of observations, as shown in the zoomed-in panels. A telluric transmittance model (gray) is fitted with PSG, adopting the atmospheric and climatological repository MERRA2 (Gelaro et al. 2017). Although in the clear, the R2 line was within the noise envelope. The P1, P2, and P3 lines were also detected. In all the plots, we show the total fluorescence model in red.

### 3. Results

#### 3.1. Molecular Spatial Profiles

Molecular spatial profiles for the brightest lines ( $\text{H}_2\text{O}$ , HCN,  $\text{C}_2\text{H}_6$ , and CO) and for dust are reported in Figure 3, and related information is listed in Table 2. Each molecule is displayed with a distinct color as defined in the previous

section, and this strategy is retained throughout the manuscript to assist visualization.

Molecular spatial profiles for comet/Leonard appear shifted relative to the dust profiles, and such shifts are always observed toward the sunward direction. This is not the first time we have observed such large shifts; they have been recorded in many comets, such as C/2020 F3 NEOWISE, C/2013 V5 Oukaimeden, C/2007 W1 Boattini, and 103P/Hartley 2 (Villanueva et al. 2011a; DiSanti et al. 2018; Faggi et al. 2021; Mumma et al. 2011). As discussed in Faggi et al. (2021), shifts of the molecular spatial profiles have either been interpreted as evidence for a large amount of gas sublimating from icy grains at that specific nucleocentric distance (which probably dominated the outflowing of the vapor released directly from the nucleus), or they can be interpreted as the possible presence of jets in the coma. Comet/Leonard was followed by many amateur astronomers, and the available photometry showed a very convoluted and constantly evolving coma during its approach to perihelion, with many outbursts recorded as shown in the composite image in Figure 1. In the image, photometric evolution of the dust coma and tail from 2021 December 19 to 2022 January 5 is reported (credit: Rolando Ligustri, CARA/UAI). From our molecular spatial profiles, we cannot quantify the nature of such convoluted phenomena, nor can we distinguish among the possible sources of such large shifts, but we can certainly identify that the gas release was not dominated solely by nucleus outgassing. The spatial profiles for the three organic species that we could analyze (HCN, C<sub>2</sub>H<sub>6</sub>, and CO) showed not quite the same gas-to-dust shifts, as reported in Table 2. On January 8 the H<sub>2</sub>O profile had a shift of  $-1$  pixel relative to the dust, while both the CO and C<sub>2</sub>H<sub>6</sub> profiles showed the same shift of  $-2$  pixels; on January 8 both H<sub>2</sub>O and HCN profiles had the same shift of  $-8$  pixels relative to the dust, while C<sub>2</sub>H<sub>6</sub> had a shift of  $-6$  pixels. However, we can clearly observe that spatial profiles for the three organic species faithfully follow the direction of the water release toward the sunward direction within small shifts (around or less than 2 pixels), which are within the point-spread function seeing of the observations. This is possibly indicating that we do not observe separate relationships for polar and apolar molecules, as would appear if the two ice phases were spatially separated when contributing to the overall gas production.

Differences are seen in the dust profiles extracted in L1c/order 175 ( $\sim 2.9 \mu\text{m}$ ) and Lp1c/order 155 ( $\sim 3.3 \mu\text{m}$ ). The continuum flux density, which is composed of both the reflected Sun light and the thermal emission components, is more extended in L1c than in Lp1c. The reason for these differences could be multifaceted and could be related to the particle size distribution of the dust/icy particles, their composition, and also the effective phase function. The dramatic change in separation seen for water and for ethane relative to dust on January 9 compared with January 8 (Table 2 and Figure 3) could result from a change in volatile release on the two dates during the outburst.

We adopted the standard ABBA nodding on-slit technique to observe comet/Leonard, even though it showed a very large and extended coma. Considering the extended nature of the emission and the iSHELL 15'' slit length, A–B differencing may lead to oversubtraction of the cometary signal in the inner region of the slit. However, it is important to consider that oversubtraction between the two beams, in principle, occurs in all cometary observations, and the relative impact of this effect is typically proportional to the cometary nucleocentric distance

as  $\sim 1/\rho$ . Thus, considering the 7'' distance of the iSHELL beam switching, effectively this effect was greatly reduced at such distances, and its impact was marginal on the nucleocentric extracted production rates. While an impact on the spatial profile analysis is present (e.g., we identify truncated profiles—gray regions in Figure 3.), this effect is not substantial and did not prevent a complete analysis.

### 3.2. Molecular Production Rates

A total of 14 molecular species were detected in comet/Leonard: 11 primary volatiles (H<sub>2</sub>O, HCN, NH<sub>3</sub>, CO, C<sub>2</sub>H<sub>2</sub>, C<sub>2</sub>H<sub>6</sub>, CH<sub>4</sub>, CH<sub>3</sub>OH, H<sub>2</sub>CO, OCS, and HCl), and 3 product species (CN, NH<sub>2</sub>, OH). To compute molecular production rates, we first retrieved the centered production rates ( $Q_c$ ), which were computed from the extracted spectra, centered at the offset position corresponding to the peak of the spatial profile. When the offset is zero (no gas shift relative to the dust), the centered production rates correspond to the nucleus-centered production rates ( $Q_{\text{nuc}}$ ). Centered production rates were retrieved from each rovibrational detected line, comparing the calibrated fluxes (corrected for the terrestrial transmittance at the Doppler-shifted line frequencies) with the fluorescence efficiencies ( $g$ -factors [photons molecule<sup>-1</sup> s<sup>-1</sup>]) obtained at specific rotational temperature  $T_{\text{rot}}$  (K), as derived from the quantum mechanical fluorescence models developed by the Goddard team (DiSanti et al. 2006; Villanueva et al. 2011b, 2012a, 2012b, 2013b).

The  $\chi^2$  minimization process, based on well-established Levenberg–Marquardt nonlinear minimization fitting (Villanueva et al. 2011a), was adopted to retrieve rotational temperatures ( $T_{\text{rot}}$ ) and molecular production rates. In this approach, all the detected molecular species are fitted simultaneously with the continuum affected by the telluric absorptions, order by order. Production rates were also compared with results obtained from the new Goddard Python data reduction pipeline, which is now under testing and benchmarking, which adopts the Optimal Estimation method integrated in the PSG Retrieval package (Villanueva et al. 2018), which operates by fully integrating the Geometry, the Radiative Transfer, the Continuum, and the Generator modules. Detailed information on the PSG Retrieval Package and on the intermodule's operability can be found in the PSG Handbook (G. L. Villanueva et al. 2023, in preparation). Retrieved values with the two techniques mostly agree within uncertainties. As examples, the water production rate on 2021 December 20, in order 179 of the L1c setting, was retrieved to be  $Q(\text{H}_2\text{O}) \sim (3.94 \pm 0.09) \times 10^{28} [\text{s}^{-1}]$  adopting the custom IDL data package and to be  $Q(\text{H}_2\text{O}) \sim (3.84 \pm 0.09) \times 10^{28} [\text{s}^{-1}]$  adopting the new Python pipeline; the ethane production rate on 2022 January 8, in order 155 of the Lp1c setting, was retrieved to be  $Q(\text{C}_2\text{H}_6) \sim (5.78 \pm 0.06) \times 10^{26} [\text{s}^{-1}]$  adopting the custom IDL data package and to be  $Q(\text{C}_2\text{H}_6) \sim (5.73 \pm 0.06) \times 10^{26} [\text{s}^{-1}]$  adopting the new Python pipeline; and finally, the hydrogen cyanide production rate on 2022 January 9, in order 172 of the L1c setting, was retrieved to be  $Q(\text{HCN}) \sim (4.39 \pm 0.25) \times 10^{25} [\text{s}^{-1}]$  adopting the custom IDL data package and to be  $Q(\text{HCN}) \sim (4.46 \pm 0.25) \times 10^{25} [\text{s}^{-1}]$  adopting the new Python pipeline. Differences might arise from the subpixel alignments when straightening the frames, from the way the two fitting methodologies are handling the telluric subtraction, and from how accurate the frequency calibration is performed since it requires user intervention. In Table 3, a

**Table 3**  
Retrieved Rotational Temperatures, Production Rates, and Mixing Ratios for Primary Volatiles in Comet/Leonard

Date	Spectral Setting	Molecule	$T_{\text{rot}}^a$ (K)	$Q_c^b$ ( $10^{25} \text{ s}^{-1}$ )	$Q_{\text{scale}}^c$	$Q_{\text{tot}}$ ( $10^{25} \text{ s}^{-1}$ )	Mixing Ratio <sup>d</sup> (%)
20 Dec 2021	L1c	H <sub>2</sub> O	95 ± 1	4029.87 ± 33.98	2.10 ± 0.27	8 462.73 ± 1211.07	100
		HCN	[95]	4.19 ± 0.15		8.79 ± 1.30	0.10 ± 0.01
		C <sub>2</sub> H <sub>2</sub>	[95]	3.75 ± 0.26		7.88 ± 1.26	0.09 ± 0.01
		NH <sub>3</sub>	[95]	<13.77		<57.29	<0.34
8 Jan 2021	M1	H <sub>2</sub> O	120 ± 1	23 934.60 ± 174.13	1.78 ± 0.04	41 122.31 ± 1028.53	100
		CO	[120]	247.07 ± 3.48		424.50 ± 11.78	1.03 ± 0.02
		OCS	[120]	26.13 ± 1.05		44.89 ± 2.10	0.11 ± 0.01
	Lp1	C <sub>2</sub> H <sub>6</sub>	120 ± 3	59.41 ± 0.48	1.65 ± 0.09	98.17 ± 5.42	0.25 ± 0.01
		CH <sub>3</sub> OH	[120]	<17.05		<28.57	<0.07
		CH <sub>4</sub>	[120]	49.40 ± 3.45		81.64 ± 7.25	0.21 ± 0.02
		H <sub>2</sub> CO	[120]	34.35 ± 1.04		56.77 ± 3.54	0.14 ± 0.01
		HCl	[120]	5.15 ± 0.49		8.50 ± 0.94	0.02 ± 0.01
9 Jan 2021	L1c	H <sub>2</sub> O	93 ± 1	3 694.37 ± 35.86	2.03 ± 0.17	7 522.50 ± 643.33	100
		HCN	[93]	4.10 ± 0.19		8.35 ± 0.81	0.11 ± 0.01
		C <sub>2</sub> H <sub>2</sub>	[93]	3.03 ± 0.31		6.17 ± 0.83	0.08 ± 0.01
		NH <sub>3</sub>	[93]	<16.0		<32.65	<0.43
	L3	C <sub>2</sub> H <sub>6</sub>	120 ± 3	9.24 ± 0.22	1.77 ± 0.14	16.42 ± 1.36	0.25 ± 0.01
		CH <sub>3</sub> OH	[120]	<8.13		<15.31	<0.22
		CH <sub>4</sub>	[120]	5.80 ± 0.41		10.31 ± 1.10	0.16 ± 0.01
		HCl <sup>e</sup>	[120]	1.78 ± 0.34		2.94 ± 0.58	0.05 ± 0.01

#### Notes.

<sup>a</sup> Rotational temperatures are reported. When an accurate rotational temperature was not derived, due to the low signal-to-noise ratio or reduced number of detected lines, we adopted a fixed value of  $T_{\text{rot}}$ , chosen based on the most sensitive measurement for that night. Adopted  $T_{\text{rot}}$  are reported in squared brackets. We also adopted a fixed value of  $T_{\text{rot}}$  when the error ( $\pm 1\sigma$ ) retrieved from the excitation analysis method was larger than 30 K.

<sup>b</sup> Centered production rates (or nucleus centered when gas shift is zero) are reported in this column. Detections lower than  $3\sigma$  are reported here as upper limits. Confidence limits reported in this column correspond to the stochastic noise only. Systematics are included in the total production rate  $Q_{\text{tot}}$ , after applying slit-loss correction ( $Q_{\text{scale}}$ ).

<sup>c</sup> The growth factor ( $Q_{\text{scale}}$ ) is a correction factor that primarily accounts for the loss of flux due to the atmospheric seeing. Values for each spectral setting are reported and evaluated on brightest lines; see spatial profile section.

<sup>d</sup> Mixing ratios relative to measured water are evaluated relative to the centered production rates  $Q_c$  in the fifth column.

<sup>e</sup> Despite a single line being detected (R1 at rest frequency 2925.896  $\text{cm}^{-1}$ ) in both order 151 and order 152 of setting L3, we consider this detection as a confirmative of the previous day.

summary of retrieved molecular production rates is reported. The total production rate ( $Q_{\text{tot}}$ ) for each species is obtained by applying to each centered (or nucleus centered when offset is zero) production rate the slit-loss correction, as follows:  $Q_{\text{tot}} = Q_c \times Q_{\text{scale}}$  (evaluated from the spatial profile analysis). Molecular abundances (mixing ratios) are computed as the ratio between the total production rates for the trace species and for water [ $Q_{\text{tot}}(x)/Q_{\text{tot}}(\text{H}_2\text{O})$ ], and values are shown in the last column of Table 3. Discussion of their significance is addressed in Section 4.

#### 3.2.1. Detection of HCl

As introduced in Section 2, detections of the 1–0 band of HCl were attempted in orders 146, 147, 148, 151, and 152 of setting Lp1 on January 8 and orders 151 and 152 of setting L3 on January 9.

On both settings Lp1 and L3, one faint line of HCl falling in order 151 was clearly identified (R1 at the rest frequency of 2925.8965  $\text{cm}^{-1}$ ), and it was seen again in order 152. A second line in order 151 was expected (R0 at  $\sim 2906.2467 \text{ cm}^{-1}$ ), but it fell into telluric absorption, preventing its identification. Together with the R1 line at  $\sim 2925.897 \text{ cm}^{-1}$ , a third HCl line in order 152 (R2 at rest 2944.9134  $\text{cm}^{-1}$ ) was searched, but it appeared to be within the noise envelope. The R1 line at 2925.896  $\text{cm}^{-1}$  was detected for 2 consecutive days, and on each day in both orders 151 and 152, as shown in the zoomed-in panels of Figure 2. Three additional lines of the

P-branch were searched in setting Lp1: the HCl line P3 was identified in order 146 at rest frequency 2821.568  $\text{cm}^{-1}$ , the HCl line P2 was identified in order 147 at rest frequency 2843.624  $\text{cm}^{-1}$  and the HCl line P1 was identified in order 148 at rest frequency 2865.098  $\text{cm}^{-1}$ . These spectral orders were not sampled in setting L3, so we could not test the P1, P2, and P3 line identification on the following day. Retrieved HCl values, for each day, are reported in Table 3 and discussed in the related caption.

HCl spectroscopic information and modeled  $g$ -factors [ $\text{s}^{-1}$ ] at  $T^{\text{rot}} = 120$  [K] are also reported in Table 4. Abundance ratios of HCl relative to water provide a mean value of  $0.03\% \pm 0.01\%$ , which seems to be consistent with previous measurements in comets; see Section 4. Our interpretation is based on an assumption of a rotational population characterized by a temperature of 120 K. Ultimately, the nondetection of the R2 line at  $\sim 2944.913 \text{ cm}^{-1}$  on either of the two dates may suggest the need of special modeling for this molecule (e.g., fluorescence equilibrium). Since we have a robust detection of four lines (P1, P2, P3, and R1) on January 8, we consider the detection of a single line (R1) on the January 9 confirmative as well.

## 4. Discussion

### 4.1. Overall Chemical Composition

Molecular mixing ratios in comet/Leonard are reported in Table 3 and graphed in Figure 4. In the figure, histograms

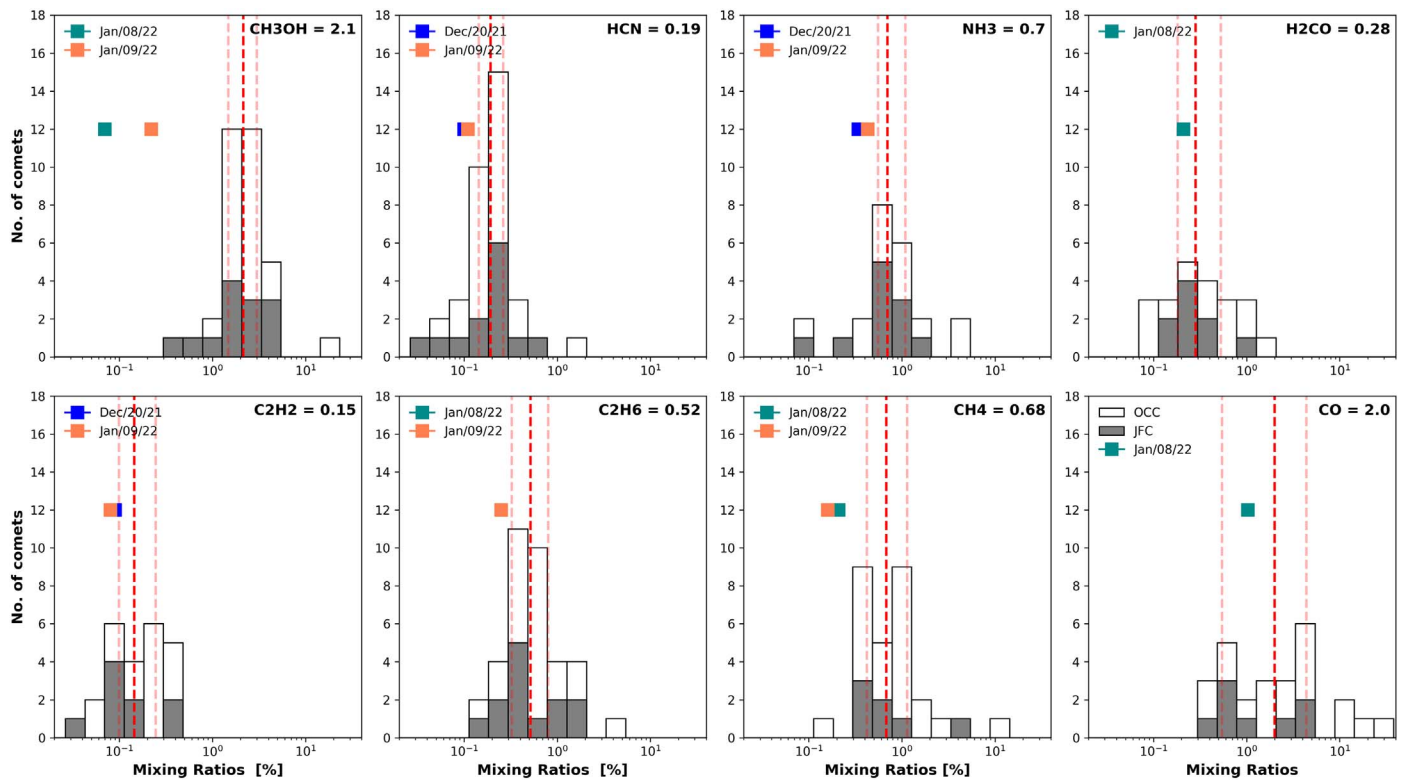


**Figure 4.** Molecular mixing ratios in comet/Leonard and compared to the full cometary database; see Lippi et al. (2021) and Faggi et al. (2021).

**Table 4**  
HCl Spectroscopic Information

Rest Frequency ( $\text{cm}^{-1}$ )	$E_{\text{up}}$ ( $\text{cm}^{-1}$ )	$g$ -factor ( $\text{s}^{-1}$ )	Rovibration ID	iSHELL/Lp1c Spectral Order
2906.2467	20.2703	1.620462E-05	$\nu'-\nu'' = 1-0 R_0$	151
2925.8965	60.7984	2.193020E-05	$\nu'-\nu'' = 1-0 R_1$	151,152
2944.9134	121.5592	1.809616E-05	$\nu'-\nu'' = 1-0 R_2$	152
2865.0977	0.000	1.974556E-05	$\nu'-\nu'' = 1-0 P_1$	148
2843.6242	20.2703	3.281070E-05	$\nu'-\nu'' = 1-0 P_2$	147
2821.5684	60.7983	3.357846E-05	$\nu'-\nu'' = 1-0 P_3$	146

showing the distribution of mixing ratios, relative to water, for the eight primary molecular species are reported in order of sublimation temperature. Jupiter-family comets are shown as gray shaded histograms, while Oort cloud comets are shown in white. The vertical red dashed line, in each panel, identifies the median value of the distribution, which is also reported in the upper right corner, while light-red vertical dashed lines identify the 25th and 75th percentiles of the distribution.

Thirty-eight comets are included in the database—the 27 Oort Cloud comets described in our previous work (Faggi et al. 2021; Lippi et al. 2021 and references therein), and the 11 Jupiter-family comets reported in recent taxonomical studies (Dello Russo et al. 2016 and Lippi et al. 2020, 2021) with the addition of 46P/Wirtanen (Bonev et al. 2021; Roth et al. 2021).

Molecular abundances in comet/Leonard, from the first data acquired on 2021 December 20 to the others on January 8 and 9, appear to be consistently overall depleted relative to the median value of the total comet sample distribution, as shown in Figure 4. Methanol appears to be strongly depleted and well below the 25th percentile of the distribution, showing probably one of the strongest depletions ever measured, followed by

methane, ethane, and the other molecules, excepting CO and  $\text{H}_2\text{CO}$ , which appear mildly depleted relative to the median value, but their abundance is still within the 25th percentile of the distribution.

Additional and complementary near-infrared observations obtained with CRIFRES+/VLT performed within the time frame of our observations, on 2021 December 28 and 31 and on 2022 January 3, confirmed the observed depletion of almost all chemical inventory in comet/Leonard. Discussion is presented in a related paper (M. Lippi et al. 2023, in preparation).

#### 4.2. Significance of Strong $\text{CH}_3\text{OH}$ Depletion

Following the current understanding of chemical processes in the interstellar medium (ISM), molecules can be produced or destroyed through either gas-phase reactions or dust grain-surface chemistry, and during these processes both UV radiation and cosmic-ray bombardment play an important role (Cuppen et al. 2017; Simončič et al. 2020). The charge transfer between  $\text{H}^+$  and O and between C and N atoms leads to first molecular syntheses, via sequences of ion–molecule and

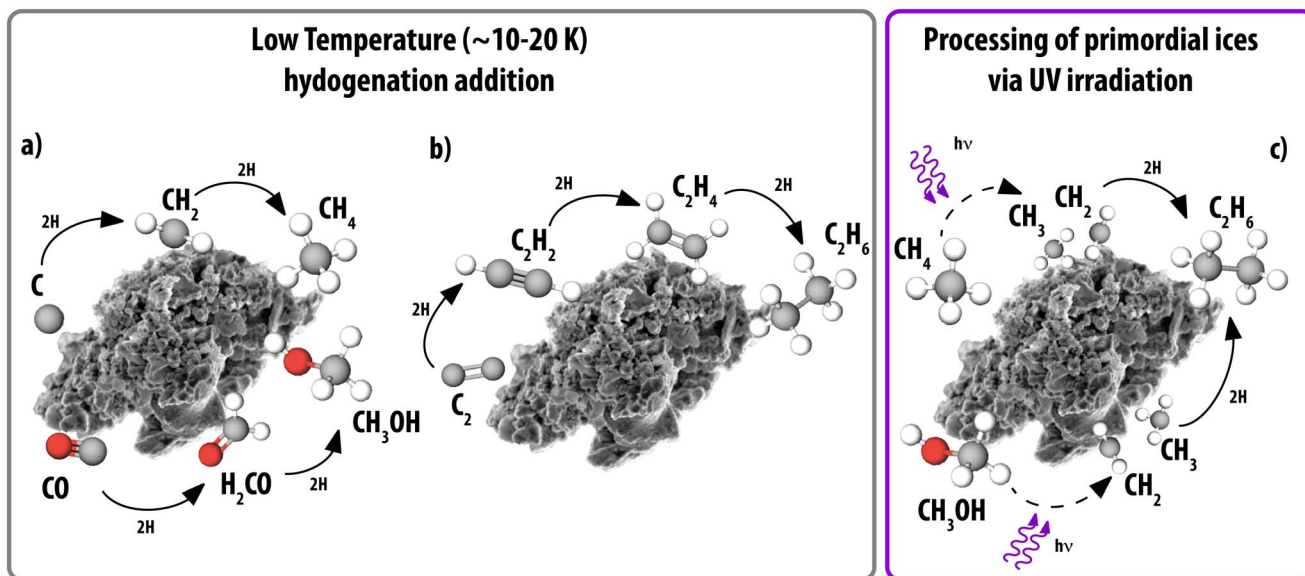


**Figure 5.** Summary of grain-surface chemistry. (a, b) Pathways to produce methane (CH<sub>4</sub>), methanol (CH<sub>3</sub>OH), and ethane (C<sub>2</sub>H<sub>6</sub>) via hydrogenation addition reactions in primordial cometary grains at low formation temperatures (10–20 K), starting from CO, atomic carbon, and molecular carbon (C<sub>2</sub>). (c) Ethane (C<sub>2</sub>H<sub>6</sub>) formation processes by two pathways involving UV irradiation and hydrogenation addition reactions on the cometary icy mantles starting from the destruction of methane (CH<sub>4</sub>) and methanol (CH<sub>3</sub>OH).

dissociative recombination reactions involving H<sub>2</sub>, and to the production of OH, CO, and N<sub>2</sub> as the most abundant molecules after H<sub>2</sub> (Nuth et al. 2006). While molecules such as CO are mostly formed in the gas phase, some other simple but key molecules such as H<sub>2</sub>, H<sub>2</sub>O, CH<sub>4</sub>, NH<sub>3</sub>, and CH<sub>3</sub>OH are instead thought to be mainly synthesized through grain-surface processes (Herbst & van Dishoeck 2009; Tielens 2010). At low temperatures ( $T \leq 30$  K), the “freezeout” mechanism allows accretion of hypervolatile species (e.g., CO, N<sub>2</sub>) on grain surfaces, and recombination of highly mobile atomic hydrogen with other species then plays a very important role in enhancing the molecular complexity of ice mantles (Charnley & Rodgers 2008). For example, as illustrated in Figure 5(a), H-addition could explain rich methane abundances via hydrogenation of C leading to CH<sub>2</sub> and finally to CH<sub>4</sub> (Krasnokutski et al. 2016; Henning & Krasnokutski 2019), or it could explain rich methanol abundances via hydrogenation of CO leading to H<sub>2</sub>CO and finally to CH<sub>3</sub>OH (Watanabe et al. 2003, 2004). Methanol and methane abundances are therefore usually indicative of strong dust grain chemistry because it does not have any efficient gas-phase formation chemistry known so far (Garrod & Herbst 2006; Geppert et al. 2006).

Protoplanetary disks are predominantly made of molecular hydrogen (H<sub>2</sub>), helium, and dust particles with some trace amounts of CO and other molecular species (e.g., Henning & Semenov 2013; Dutrey et al. 2014). Gas-phase and grain-surface chemistry in protoplanetary disks is thought to be mainly driven by photochemical reactions and dust temperature gradients. As recently summarized in Ruaud & Gorti (2019), the icy disk presents three distinct chemical regions: (1) the inner midplane region, which has low far-UV fluxes coming from the ISM and dust at ~15 K that lead to the formation of complex organic molecules (COMs); (2) the outer midplane region, characterized by higher far-UV fluxes and colder dust grains, where hydrogenation reactions highly dominate; and (3) the molecular layer that lies above the icy midplane but below the water condensation front, where photodissociation of ices affects gas-phase compositions. Understanding the

grain-surface chemistry is critical to the interpretation of protoplanetary disk conditions and to understanding the chemical composition of the solid material from which our planetary system formed (Marboeuf et al. 2014; Mordasini et al. 2016). In the past decade, many theoretical models have been built to study the physics and chemistry of protoplanetary disks, but astronomical observations of such objects, especially at near-IR wavelengths, remain difficult, and relatively few molecules can be observed and studied in detail (Banzatti et al. 2022).

Cometary observations, though, could be the bridge in understanding our protosolar disk conditions and evolution. Cometary ices might indeed retain heritage signatures from the prestellar core/ISM phase era, in the midplane region where they formed, as well as signatures of the processing that they experienced in the formative locations during the protoplanetary disk midplane evolution. According to disk models (Bergin et al. 2007; Cleeves et al. 2014; Bergin & Cleeves 2018; Eistrup et al. 2019), we expect indeed to observe different signatures of processing on cometary ices according to the different birthplace locations in the disk midplane.

The strong methanol depletion, together with the general depletion of the organic inventory observed in comet/Leonard, (i) might be an indication of warm nebular temperatures at which the interstellar ices condensed, (ii) could point to a region of the presolar nebula where CO was mostly depleted and chemical complexity on interstellar grains via surface chemistry was not efficiently enhanced, or (iii) might be a possible indication of thermal processing in the disk midplane, where loss of interstellar ices shaped the final composition of the ices that assembled into cometary nuclei. As discussed in Mumma et al. (2003), apolar species such as CH<sub>4</sub>, C<sub>2</sub>H<sub>6</sub>, and C<sub>2</sub>H<sub>2</sub> and molecules with small dipole moment, such as CO, are more volatile than hydrogen-bonded ices of polar species, such as CH<sub>3</sub>OH, H<sub>2</sub>CO, and HCN. Hence, if thermal processing in the disk midplane was responsible for shaping comet/Leonard composition, we would expect that

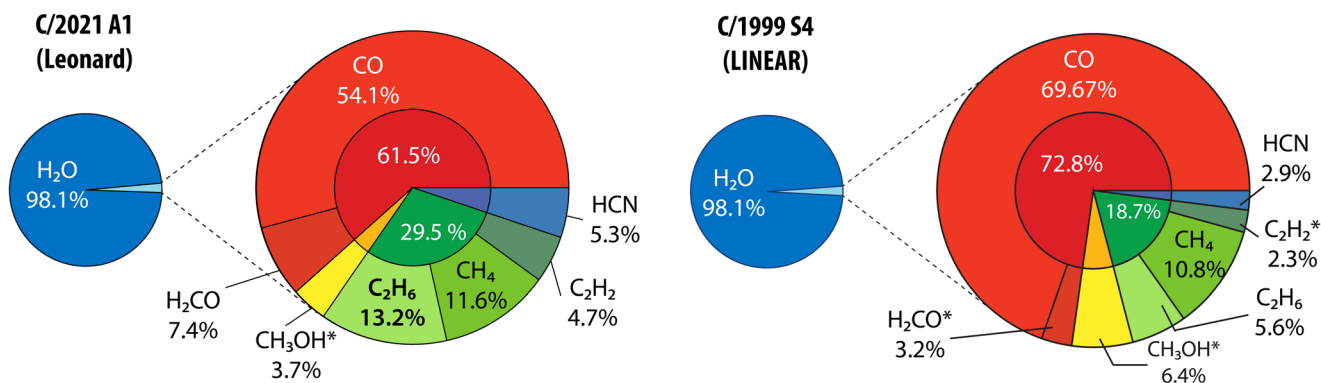


Figure 6. Comparison of comet/Leonard and C/1999 S4 (LINEAR) pie charts.

hypervolatile species such as CO, CH<sub>4</sub>, and C<sub>2</sub>H<sub>6</sub> would have larger depletions than methanol, but this is not the case.

Moreover, since CH<sub>3</sub>OH and HCN have similar volatility, and assuming a simplified view in which thermal processing is the sole factor shaping the chemical inventory in comet/Leonard, we would then expect that their abundances would be similarly depleted, but methanol is much more strongly depleted than HCN. This result points to a possible nebular origin for comet/Leonard precometary ices where CO was probably depleted and grain-surface chemistry was perhaps not particularly efficient. However, temperature is not the sole relevant factor controlling ice processing, and photochemical processing in hot regions of the molecular cloud might also have played an important role in the observed composition, destroying methanol in the gas-phase chemistry, after its thermal desorption. Or maybe a selective loss of nuclear ices during the outbursts that occurred before disruption might also have played a role. This unique chemical composition observed in comet/Leonard is puzzling, and a definitive explanation cannot be provided.

#### 4.3. Tracing the Ethane Formation

Cold  $\sim 10$  K surface chemistry of C<sub>2</sub>H<sub>2</sub> with H atoms results in hydrocarbons, such as C<sub>2</sub>H<sub>4</sub> and C<sub>2</sub>H<sub>6</sub>, as shown in Figure 5(b), and it also leads to the formation of COMs (Tielens 1992; Hiraoka et al. 2000b, 2000a; Fuchs et al. 2009; Kobayashi et al. 2017; Chuang et al. 2020). However, if CH<sub>3</sub>OH and CH<sub>4</sub> ices are processed by UV radiation, as shown in Figure 5(c), their products can be methyl and methylene highly active radicals (CH<sub>3</sub>, CH<sub>2</sub>), which quickly react to form species such as C<sub>2</sub>H<sub>6</sub> (Gerakines et al. 2001).

In comet/Leonard, both C<sub>2</sub>H<sub>2</sub> and C<sub>2</sub>H<sub>6</sub> are mildly depleted, perhaps due to the strong depletion of methanol and methane or perhaps because C<sub>2</sub>H<sub>2</sub> (which formed via warm photospheric gas reactions of atomic C with H<sub>2</sub>) did not efficiently condense, pointing again toward the direction of a possible warm formation region in the protosolar nebula, for comet/Leonard's precometary ices.

#### 4.4. Comparison with C/1999 S4 (LINEAR)

The chemistry here discussed for comet/Leonard presents similarities to the detected molecular abundances in comet C/1999 S4 (LINEAR), hereafter 99S4, (Mumma et al. 2001; Bockelee-Morvan et al. 2001; and reanalysis by Lippi et al. 2021).

Methanol was not detected in 99S4, and its upper limit relative to water was  $<0.19$  (Lippi et al. 2021), which is a value of about a factor of 10 lower than the median reference value (2.1%) found in a sample of  $\sim 30$  comets. Carbon monoxide, ethane, and methane were detected, but with very weak lines when compared to the strong OH prompt emission lines, and this pointed to their depletion relative to water. Their updated mixing ratios are reported to be  $1.36\% \pm 0.32\%$ ,  $0.11\% \pm 0.02\%$ , and  $0.22\% \pm 0.06\%$ , respectively (Lippi et al. 2021).

As discussed in Mumma et al. (2001) and later in Lippi et al. (2021), the strong methanol depletion observed in comet 99S4 was interpreted as a sign of condensation of cometary ices at moderately high nebular temperatures and probably a consequent relocation in a warm region of the protoplanetary disk. A similar composition is observed in comet/Leonard, and in Figure 6(a) graphical representation of comet A1 Leonard versus 99S4 LINEAR is shown.

The presented pie charts follow the classification as discussed in Lippi et al. (2021), where the inner level of each pie groups the molecules following their chemical functional groups, i.e., in red carbonyl and aldehyde groups (CO and H<sub>2</sub>CO), in yellow alcohol group (CH<sub>3</sub>OH), in green hydrocarbon group (C<sub>2</sub>H<sub>6</sub>, CH<sub>4</sub>, and C<sub>2</sub>H<sub>2</sub>), and in blue nitrile group (HCN), while the outer level lists each molecular species separately. In Lippi et al. (2021), the authors classified comets into four groups following the pie chart representation, and both comet A1 Leonard and 99S4 LINEAR belong to group 1, which collects comets whose composition suggests possible formation in a warm region of the protoplanetary disk midplane, where CH<sub>3</sub>OH and hydrocarbons might not be efficiently produced (Garrod & Herbst 2006; Geppert et al. 2006). Following this classification, Lippi et al. (2021) located comet 99S4 as formed perhaps at distances within 5–17 au, where nebular signatures in its ices were not substantially altered.

#### 4.5. The Chemistry of HCl

Cometary ices are shaped and formed by the different stages of their formative path. Some molecules are probably better indicators of the interstellar chemistry, while others might trace the formative region in the protoplanetary disk. Measurements of HCl in cometary comae are very limited. Upper limits for the HCl abundance relative to water were retrieved to be 0.011% and 0.22% for comet 103P/Hartley 2 and C/2009 P1 (Garradd) at 626 GHz and 1232 GHz, respectively (Bockelee-Morvan et al. 2014). In 67P/Churyumov–Gerasimenko, investigations of the halogen-bearing compounds conducted

with the ROSINA mass spectrometer on board ESA's Rosetta spacecraft showed that the elemental abundance of Cl/O varied between 0.02% and 0.05% (Hässig et al. 2015; De Keyser et al. 2017). While recognizing that elemental O abundance in the coma might come from H<sub>2</sub>O, CO<sub>2</sub>, CO, and O<sub>2</sub>, the authors assumed H<sub>2</sub>O abundance to be a good proxy for the elemental O abundance, after showing that HCl varied in sync with water. Solar abundances for Cl/O were estimated to be  $\sim 0.065\%$  (Asplund et al. 2009), and the HCl mixing ratio relative to water measured in comets 67P/C-G, C/2009 P1 (Garradd), 103P/Hartley 2, and comet/Leonard appears to be depleted relative to the primordial solar system (Cl/O) abundance.<sup>5</sup>

In dense molecular clouds, which can be representative of the presolar cloud conditions, halogens, including chlorine, react with H<sub>2</sub>, forming hydrogen halides such as HF, HCl, and HBr (Neufeld & Wolfire 2009); it is therefore natural to think that hydrogen halides can be the principal reservoirs of halogens in protostellar clouds (Dalgarno et al. 1974; Jura et al. 1974). HCl is found to be strongly depleted in dense molecular clouds, relative to solar abundances, suggesting that an efficient freezeout mechanism onto grain surfaces is in place in such cold environments (Peng et al. 2010; Emprechtinger et al. 2012). Moreover, the first gas-grain chemical model for chlorine estimated that in protostellar cores at least 90% of the full chlorine inventory is locked in HCl ice (Kama et al. 2015). However, the detection of abundant ammonium salts in comets (including NH<sub>4</sub><sup>+</sup>Cl<sup>-</sup> in 67P/Churyumov-Gerasimenko; Altwegg et al. 2020) and their likely origin in interstellar dense clouds (Bergner et al. 2016) could also probably explain the difference.

As discussed at the beginning of this section, comets might contain pristine protostellar material, so their retrieved molecular abundances could reflect information about their formative regions and provide hints about hydrogen halide abundances in the protosolar cloud formative stage. The strong depletion observed so far in four comets might point either to a possible prestellar origin where halogen deficit in the gas phase reflects the possible presence of hydrogen halides on dust grains (Kama et al. 2015) or to HCl not being the sole reservoir for Cl in the solar nebula, in agreement with recent observations in L1157-B1 shock, where both volatile and refractory components are enhanced, and where the recovered HCl abundance was lower than expected (Codella et al. 2012). This might also point again to the abundance of ammonium salts, including NH<sub>4</sub><sup>+</sup>Cl<sup>-</sup>, in comets.

#### 4.6. Detection of OCS

Detections of OCS were obtained on 2022 January 8 in order 106 of setting M1 of iSHELL (Figure 2), near 2054 [cm<sup>-1</sup>]. Secure detections of OCS were previously recorded in a small sample of comets, with a total of 10 detections and five upper limits reported so far (Saki et al. 2020, and references therein). Despite the limited sample, a reference value of 0.126%  $\pm$  0.034% was reported as an unweighted mean of the distribution,

<sup>5</sup> As discussed in Bockelee-Morvan et al. (2014), the comparison of the HCl/H<sub>2</sub>O abundance with the Cl/O solar abundance has the strong assumption of considering HCl/H<sub>2</sub>O to be representative of Cl/O bulk abundances in cometary ices. This can be inaccurate since other oxygen-bearing compounds are significantly present in cometary ices, such as CO<sub>2</sub>, CO, and CH<sub>3</sub>OH. Hence, this comparison likely overestimated the Cl/O abundances in cometary ices, when using the abundances relative to water.

and the OCS abundance in comet/Leonard (0.11%  $\pm$  0.01%) appears to be consistent with the reference value.

The significance of investigating sulfur-bearing species is related to their astrobiological implications. For example, OCS acts as a catalyst in the peptide synthesis, playing a fundamental role in biochemistry (Brosnan & Brosnan 2006; Chen et al. 2015), so investigation of its molecular abundance in comets allows us to expand our understanding of its chemistry and evolutionary processing in precometary ices, in the framework of solar system formation and delivery of S-bearing molecules to early Earth.

Sulfur-bearing species have been broadly observed in the ISM and are thought to be tracers of chemical evolution and processing in dark clouds. For example, the ratio of radical CCS to NH<sub>3</sub> is believed to be representative of the chemical evolution of a dark cloud core associated with the cloud contraction and formation of low-mass stars, where CCS is observed to be abundant in the early formation, while NH<sub>3</sub> abundance increases in the later evolutionary stages (Suzuki et al. 1992). Molecules such as SO, SO<sub>2</sub>, and OCS are instead associated with the temperature variation along shocks in star-forming regions (Esplagues et al. 2014), and they are thought to track signatures of X-ray irradiation and warm surface grain processing (Charnley 1997; Stäuber et al. 2005).

The reaction  $S + CO \rightarrow OCS + h\nu$  was identified to be particularly important for the prediction of gas-phase OCS abundances by chemical models of dark clouds (Loison et al. 2012). But recently updated ab initio calculations for this process revealed a new, significantly smaller rate for this reaction, when compared to previous astrochemical models, dramatically changing the OCS gas-phase abundance predicted by chemical models for dark clouds. Moreover, disagreements with dark cloud observations (e.g., TMC-1 and L134N) suggest that OCS may be preferentially formed on grain surfaces (Palumbo et al. 1997, and references therein). The observation of solid OCS on interstellar ices further supports this hypothesis (Lovas & Dragoset 2004).

Laboratory investigations demonstrated the efficient solid-state formation of OCS, in proton-irradiated water-free and water-dominated ices, containing a mixture of CO or CO<sub>2</sub> and H<sub>2</sub>S or SO<sub>2</sub>. The mechanism of OCS formation appears to mainly follow the reaction of CO with free S atoms, produced from the fragmentation of the sulfur-bearing species (Moore et al. 2007; Ferrante et al. 2008). While OCS is readily formed by irradiation, it is also destroyed on continued exposure, up to a lifetime of  $\sim 7$  million years in a cold dense interstellar cloud environment processed by cosmic-ray protons (Ferrante et al. 2008).

When compared to the observed interstellar abundances, which are close to the cosmic value (e.g., Goicoechea et al. 2006; Howk et al. 2006; Neufeld et al. 2015), in warm dense molecular clouds sulfur-bearing molecules appear highly depleted, by about three orders of magnitude (e.g., Wakelam et al. 2004; Vastel et al. 2018). This level of depletion suggests that most sulfur is locked into icy interstellar dust grains (Millar & Herbst 1990; Ruffle et al. 1999; Vidal et al. 2017; Laas & Caselli 2019).

Interestingly, this dichotomy is also observed in protoplanetary disks. The numerous detections of sulfur-bearing molecules achieved in the ISM and in comets contrast the lack of their presence in protoplanetary disks, where only CS, H<sub>2</sub>CS, and SO have been detected so far (Dutrey et al. 2011;

Guilloteau et al. 2016; Pacheco-Vázquez et al. 2016; Sakai et al. 2016; Semenov et al. 2018). This was furthermore confirmed by the recent investigations of the DM Tau protoplanetary disk, where the combination of both observations and astrochemical model constrained sulfur abundances at  $\sim 5$  [mJy] sensitivity, inferring high CS/SO and CS/SO<sub>2</sub> ratios and implying a nonsolar C/O gas-phase ratio.

The need to properly characterize the observed interstellar and protoplanetary disk sulfur-bearing species abundances triggered the development of sophisticated astrochemical models that included sulfur chemistry in both gas phase and solid phase and reproduced the predicted abundances observed on icy grains (e.g., Woods et al. 2015; Vidal et al. 2017; Vidal & Wakelam 2018; Laas & Caselli 2019). However, it is not yet fully understood whether interstellar sulfur molecules survive the different evolutionary stages of planetary formation and their interstellar abundance is preserved, or whether it is the result of the reset chemistry in the protoplanetary disk.

As shown in the ROSINA/Rosetta analysis of the 67P/Churyumov–Gerasimenko cometary ices (e.g., Altwegg et al. 2016), sulfur species present in comets, as we see in comet/Leonard, could be relics of the interstellar chemistry. Isotopic investigations could be used to constrain whether they are of interstellar or disk origin, but this would require higher instrument sensitivity and a better understanding of the disk sulfur chemistry.

## 5. Conclusions

We reported the molecular composition of comet/Leonard as revealed by high-resolution spectroscopic observations using iSHELL/IRTF. A plethora of molecules (H<sub>2</sub>O, HCN, C<sub>2</sub>H<sub>2</sub>, NH<sub>3</sub>, NH<sub>2</sub>, C<sub>2</sub>H<sub>6</sub>, CH<sub>4</sub>, H<sub>2</sub>CO, CO, OCS, and HCl) were detected over the entire observing campaign, from 2021 December 20, when the comet was at  $R_h = 0.68$  au and  $\Delta = 0.42$  au, to early 2022 January (on January 8 and 9), when the comet was at about  $R_h \sim 0.62$  au and  $\Delta \sim 1.1$  au. The comet was in outburst during the later observations.

The possible presence of icy grains in the coma was hypothesized through the interpretation of the molecular spatial profiles, which presented large shifts toward the sunward direction, relative to the dust profiles. Spatial profiles for three organic species (HCN, C<sub>2</sub>H<sub>6</sub>, and CO) were analyzed and were shown to follow the water spatial distribution. We interpreted this as indication of a nonseparate relationship of polar and apolar molecules, perhaps meaning that both icy phases were present and contributing to the overall gas production. However, we cannot provide definitive information on their distribution within the nucleus surface.

Analysis of molecular mixing ratios showed a strong methanol depletion, together with a general depletion of the organic inventory. We interpreted the observed stronger depletion of CH<sub>3</sub>OH, relative to CO, CH<sub>4</sub>, and C<sub>2</sub>H<sub>6</sub>, as evidence of interstellar/solar nebular chemistry signatures in comet/Leonard ices. Since thermal processing in the protoplanetary disk, at the location where these ices likely formed in the protosolar nebula, would affect hypervolatile species more than methanol, we would then expect largest depletions for molecules such as CO, CH<sub>4</sub>, and C<sub>2</sub>H<sub>6</sub> if processing in the disk midplane shaped comet/Leonard composition. But methanol is much more strongly depleted than HCN (which has similar volatility) and hypervolatile species. We interpreted this result as a possible indication of nebular origin for comet/Leonard

precometary ices, where CO was probably depleted and grain-surface chemistry was perhaps inhibited.

Together with strong depletion of CH<sub>3</sub>OH, detections of HCl and strong detections of OCS both support the idea of interstellar origin for comet/Leonard ices. As discussed in Sections 4.5 and 4.6, both HCl and OCS are considered to be preferentially formed via solid-phase processes in interstellar chemistry and consequently stored on grain surfaces. Both HCl and OCS are found depleted in dense molecular clouds and protoplanetary disks, suggesting that the abundances observed today in these comets might retain a signature from the ISM era. Moreover, the formation of ammonium ices in such regions may also lead to significant reductions of native HCl.

As discussed in Section 4.2, we are aware that temperature is not the sole relevant factor controlling ice processing. Any evolutionary processing that produces, for example, a selective loss of nuclear ices might also have played a role in shaping comet/Leonard's observed composition.

This work was supported by the NASA's Planetary Science Division Internal Scientist Funding Program (ISFM) through the Fundamental Laboratory Research (FLaRe) work package and the Sellers Exoplanet Environments Collaboration (SEEC) work package, by the Goddard Center for Astrobiology (GCA), and by NASA/HQ Comet Interceptor Mission funds. Data presented in this work were obtained at the NASA Infrared Telescope Facility, operated by the University of Hawai'i. We profoundly thank the staff of IRTF for the outstanding operational skills and valuable technical support during the observing campaign. The authors thank the Director and Deputy Director of the NASA InfraRed Telescope Facility for awarding time to extend our proposed date, allowing investigations of this exceptional object. We further thank Rolando Ligustri (CARA/UAI) for permission to show his images of Comet/Leonard.

The authors wish to recognize and acknowledge the very significant cultural role and reverence that the summit of Maunakea has always had within the indigenous Hawaiian community. We are most fortunate to have the opportunity to conduct observations from this mountain.

## ORCID iDs

Sara Faggi  <https://orcid.org/0000-0003-0194-5615>  
 Manuela Lippi  <https://orcid.org/0000-0001-9185-878X>  
 Michael J. Mumma  <https://orcid.org/0000-0003-4627-750X>  
 Geronimo L. Villanueva  <https://orcid.org/0000-0002-2662-5776>

## References

- Altwegg, K., Balsiger, H., Bar-Nun, A., et al. 2016, *SciA*, **2**, e1600285  
 Altwegg, K., Balsiger, H., Hänni, N., et al. 2020, *NatAs*, **4**, 533  
 Asplund, M., Grevesse, N., Sauval, J., & Scott, P. 2009, *ARA&A*, **47**, 481  
 Banzatti, A., Abernathy, K. M., Brittain, S., et al. 2022, *AJ*, **163**, 174  
 Bergin, E. A., & Cleeves, L. I. 2018, in *Handbook of Exoplanets*, Vol. 786, ed. H. Deeg & J. Belmonte (Cham: Springer), 137  
 Bergin, E. A., Aikawa, Y., Blake, G. A., & van Dishoeck, E. F. 2007, in *Protostars and Planets V*, ed. B. Reipurth, D. Jewitt, & K. Keil (Tucson, AZ: Univ. Arizona Press), 751  
 Bergner, J. B., Öberg, K. I., Rajappan, M., & Fayolle, E. C. 2016, *ApJ*, **829**, 85  
 Bockelee-Morvan, D., Biver, N., Crovisier, J., et al. 2014, *A&A*, **562**, A5  
 Bockelee-Morvan, D., Biver, N., Moreno, R., et al. 2001, *Sci*, **292**, 1339  
 Bonev, B., Dello Russo, N., DiSanti, M. A., et al. 2021, *PSJ*, **2**, 45  
 Brosnan, J. T., & Brosnan, M. E. 2006, *J. Nutr.*, **136**, 1636S  
 Charnley, S. B. 1997, *ApJ*, **481**, 396

- Charnley, S. B., & Rodgers, S. D. 2008, *SSRv*, **138**, 59
- Chen, Y.-J., Juang, K.-J., Nuevo, M., et al. 2015, *ApJ*, **798**, 80
- Chuang, K. J., Fedoseev, G., Qasim, D., et al. 2020, *A&A*, **635**, A199
- Cleeves, L. I., Bergin, E. A., O'D. Alexander, C. M., et al. 2014, *Sci*, **345**, 1590
- Codella, C., Ceccarelli, C., Bottinelli, S., et al. 2012, *ApJ*, **744**, 164
- Cuppen, H. M., Walsh, C., Lamberts, T., et al. 2017, *SSRv*, **212**, 1
- Dalgarno, A., de Jong, T., Oppenheimer, M., & Black, J. H. 1974, *ApJL*, **192**, L37
- De Keyser, J., Dhooche, F., Altwegg, K., et al. 2017, *MNRAS*, **469**, S695
- Dello Russo, N., Kawakita, H., Vervack, R. J., Jr., & Weaver, H. A. 2016, *Icar*, **278**, 301
- DiSanti, M. A., Bonev, B. P., Gibb, E. L., et al. 2018, *AJ*, **156**, 258
- DiSanti, M. A., Bonev, B. P., Magee-Sauer, K., et al. 2006, *ApJ*, **650**, 470
- Dutrey, A., Wakelam, V., Boehler, Y., et al. 2011, *A&A*, **535**, A104
- Dutrey, A., Semenov, D., Chapillon, E., et al. 2014, in *Protostars and Planets VI*, ed. H. Beuther (Tucson, AZ: Univ. Arizona Press), 317
- Eistrup, C., Walsh, C., & van Dishoeck, E. F. 2019, *A&A*, **629**, A84
- Emprechtinger, M., Monje, R. R., van der Tak, F. F. S., et al. 2012, *ApJ*, **756**, 136
- Esplugues, G. B., Viti, S., Goicoechea, J. R., & Cernicharo, J. 2014, *A&A*, **567**, A95
- Faggi, S., Villanueva, G. L., Mumma, M. J., & Paganini, L. 2018, *AJ*, **156**, 68
- Faggi, S., Mumma, M. J., Villanueva, G. L., Paganini, L., & Lippi, M. 2019, *AJ*, **158**, 254
- Faggi, S., Lippi, M., Camarca, M., et al. 2021, *AJ*, **162**, 178
- Ferrante, R. F., Moore, M. H., Spiliotis, M. M., & Hudson, R. L. 2008, *ApJ*, **684**, 1210
- Fuchs, G. W., Cuppen, H. M., Ioppolo, S., et al. 2009, *A&A*, **505**, 629
- Garrod, R. T., & Herbst, E. 2006, *A&A*, **457**, 927
- Gelaro, Ronald, McCarty, Will, Suárez, Max J., et al. 2017, *JChI*, **30**, 5419
- Geppert, W. D., Hamberg, M., Thomas, R. D., et al. 2006, *FaDi*, **133**, 177
- Gerakines, P. A., Moore, M. H., & Hudson, R. L. 2001, *JGR*, **106**, 33381
- Goicoechea, J. R., Pety, J., Gerin, M., et al. 2006, *A&A*, **456**, 565
- Guilloteau, S., Reboussin, L., Dutrey, A., et al. 2016, *A&A*, **592**, A124
- Hässig, M., Altwegg, K., Balsiger, H., et al. 2015, *Sci*, **347**, aaa0276
- Henning, T., & Semenov, D. 2013, *ChRv*, **113**, 9016
- Henning, T. K., & Krasnokutski, S. A. 2019, *NatAs*, **3**, 568
- Herbst, E., & van Dishoeck, E. F. 2009, *ARA&A*, **47**, 427
- Hiraoka, K., Sato, T., & Takayama, T. 2000a, in *IAU Symp.* 197, *Astrochemistry: From Molecular Clouds to Planetary Systems*, ed. Y. C. Minh & E. F. van Dishoeck (Cambridge: Cambridge Univ. Press), 283
- Hiraoka, K., Takayama, T., Euchii, A., Handa, H., & Sato, T. 2000b, *ApJ*, **532**, 1029
- Howk, J. C., Sembach, K. R., & Savage, B. D. 2006, *ApJ*, **637**, 333
- Jehin, E., Moulane, Y., Manfroid, J., et al. 2022, *ATel*, **15189**, 1
- Jura, M. 1974, *ApJ*, **190**, L33
- Kama, M., Caux, E., López-Sepulcre, A., et al. 2015, *A&A*, **574**, A107
- Kobayashi, H., Hidaka, H., Lamberts, T., et al. 2017, *ApJ*, **837**, 155
- Krasnokutski, S. A., Kuhn, M., Renzler, M., et al. 2016, *ApJL*, **818**, L31
- Laas, J. C., & Caselli, P. 2019, *A&A*, **624**, A108
- Lippi, M., Villanueva, G. L., Mumma, M. J., et al. 2020, *AJ*, **159**, 157
- Lippi, M., Villanueva, G. L., Mumma, M. J., & Faggi, S. 2021, *AJ*, **162**, 74
- Loison, J.-C., Halvick, P., Bergeat, A., Hickson, K. M., & Wakelam, V. 2012, *MNRAS*, **421**, 1476
- Lovas, F. J., & Dragoset, R. A. 2004, *JPCRD*, **33**, 177
- Marboeuf, U., Thiabaud, A., Alibert, Y., Cabral, N., & Benz, W. 2014, *A&A*, **570**, A35
- Millar, T. J., & Herbst, E. 1990, *A&A*, **231**, 466
- Moore, M. H., Hudson, R. L., & Carlson, R. W. 2007, *Icar*, **189**, 409
- Mordasini, C., van Boekel, R., Mollière, P., Henning, Th., & Benneke, B. 2016, *ApJ*, **832**, 41
- Mumma, M. J., & Charnley, S. B. 2011, *ARA&A*, **49**, 471
- Mumma, M. J., Bonev, B. P., Villanueva, G. L., et al. 2011, *ApJL*, **734**, L7
- Mumma, M. J., Dello Russo, N., DiSanti, M. A., et al. 2001, *Sci*, **292**, 1334
- Mumma, M. J., DiSanti, M. A., Dello Russo, N., et al. 2003, *AdSpR*, **31**, 2563
- Neufeld, D. A., Godard, B., Gerin, M., et al. 2015, *A&A*, **577**, A49
- Neufeld, D. A., & Wolfire, M. G. 2009, *ApJ*, **706**, 1594
- Nuth, J. A., III, Charnley, S. B., & Johnson, N. M. 2006, in *Meteorites and the Early Solar System II*, ed. D. S. Lauretta & H. Y. McSween, Jr. (Tucson, AZ: Univ. Arizona Press), 147
- Pacheco-Vázquez, S., Fuente, A., Baruteau, C., et al. 2016, *A&A*, **589**, A60
- Palumbo, M. E., Geballe, T. R., & Tielens, A. G. G. M. 1997, *ApJ*, **479**, 839
- Peng, R., Yoshida, H., Chamberlin, R. A., et al. 2010, *ApJ*, **723**, 218
- Rayner, J., Bond, T., Bonnet, M., et al. 2012, *Proc. SPIE*, **8446**, 84462C
- Rayner, J., Tokunaga, A., Jaffe, D., et al. 2022, *PASP*, **134**, 015002
- Roth, N., Milam, S. N., Cordiner, M. A., et al. 2021, *PSJ*, **2**, 55
- Ruad, M., & Gorti, U. 2019, *ApJ*, **885**, 146
- Ruffle, D. P., Hartquist, T. W., Caselli, P., & Williams, D. A. 1999, *MNRAS*, **306**, 691
- Sakai, N., Oya, Y., López-Sepulcre, A., et al. 2016, *ApJL*, **820**, L34
- Saki, M., Gibb, E. L., Bonev, B. P., et al. 2020, *AJ*, **160**, 184
- Semenov, D., Favre, C., Fedele, D., et al. 2018, *A&A*, **617**, A28
- Simončič, M., Semenov, D., Krasnokutski, S., Krasnokutski, Th., & Jäger, C. 2020, *A&A*, **637**, A72
- Stäuber, P., Doty, S. D., van Dishoeck, E. F., & Benz, A. O. 2005, *A&A*, **440**, 949
- Suzuki, H., Satoshi, Y., Masatoshi, O., et al. 1992, *ApJ*, **392**, 551
- Tielens, A. G. G. M. 1992, in *Chemistry and Spectroscopy of Interstellar Molecules*, ed. K. K. Bohme (Tokyo: Univ. Tokyo Press), 237
- Tielens, A. G. G. M. 2010, *The Physics and Chemistry of the Interstellar Medium* (Cambridge: Cambridge Univ. Press)
- Vastel, C., Quénard, D., Le Gal, R., et al. 2018, *MNRAS*, **478**, 5514
- Vidal, T. H. G., & Wakelam, V. 2018, *MNRAS*, **474**, 5575
- Vidal, T. H. G., Loison, J.-C., Jaziri, A. Y., et al. 2017, *MNRAS*, **469**, 435
- Villanueva, G. L., Mumma, M. J., DiSanti, M. A., et al. 2011a, *Icar*, **216**, 227
- Villanueva, G. L., Mumma, M. J., & Magee-Sauer, K. 2011b, *JGRE*, **116**, E08012
- Villanueva, G. L., DiSanti, M. A., Mumma, M. J., & Xu, L.-H. 2012a, *ApJ*, **747**, 37
- Villanueva, G. L., Mumma, M. J., Bonev, B. P., et al. 2012b, *JQSRT*, **113**, 202
- Villanueva, G. L., Magee-Sauer, K., & Mumma, M. J. 2013a, *JQSRT*, **129**, 158
- Villanueva, G. L., Mumma, M. J., Novak, R. E., et al. 2013b, *Icar*, **223**, 11
- Villanueva, G. L., Smith, M. D., Protospapa, S., Faggi, S., & Mandell, A. M. 2018, *JQSRT*, **217**, 86
- Wakelam, V., Caselli, P., Ceccarelli, C., Herbst, E., & Castets, A. 2004, *A&A*, **422**, 159
- Watanabe, N., Shiraki, T., & Kouchi, A. 2003, *ApJ*, **588**, L121
- Watanabe, N., Nagaoka, A., Shiraki, T., & Kouchi, A. 2004, *ApJ*, **616**, 638
- Woods, P. M., Occhiogrosso, A., Viti, S., et al. 2015, *MNRAS*, **450**, 1256